Anomalous pressure drop behaviour of mixed kinematics flows of viscoelastic polymer solutions: a multiscale simulation approach

ANANTHA P. KOPPOL[1],
RADHAKRISHNA SURESHKUMAR[1],
ARASH ABEDIJABERI[2] AND BAMIN KHOMAMI[2]†

[1]Department of Energy, Environmental and Chemical Engineering,
Washington University, St Louis, MO 63130, USA

[2]Materials Research and Innovation Laboratory (MRAIL) Department of Chemical
and Biomolecular Engineering, University of Tennessee,
Knoxville, TN 37996, USA

A long-standing unresolved problem in non-Newtonian fluid mechanics, namely, the relationship between friction drag and flow rate in inertialess complex kinematics flows of dilute polymeric solutions is investigated via self-consistent multiscale flow simulations. Specifically, flow of a highly elastic dilute polymeric solution, described by first principles micromechanical models, through a 4:1:4 axisymmetric contraction and expansion geometry is examined utilizing our recently developed highly efficient multiscale flow simulation algorithm (Koppol, Sureshkumar & Khomami, *J. Non-Newtonian Fluid Mech.*, vol. 141, 2007, p. 180). Comparison with experimental measurements (Rothstein & McKinley, J. *Non-Newtonian Fluid Mech.*, vol. 86, 1999, p. 61) shows that the pressure drop evolution as a function of flow rate can be accurately predicted when the chain dynamics is described by multi-segment bead-spring micromechanical models that closely capture the transient extensional viscosity of the experimental fluid. Specifically, for the first time the experimentally observed doubling of the dimensionless excess pressure drop at intermediate flow rates is predicted. Moreover, based on an energy dissipation analysis it has been shown that the variation of the excess pressure drop with the flow rate is controlled by the flow-microstructure coupling in the extensional flow dominated region of the flow. Finally, the influence of the macromolecular chain extensibility on the vortex dynamics, i.e. growth of the upstream corner vortex at low chain extensibility or the shrinkage of the upstream corner vortex coupled with the formation of a lip vortex that eventually merges with the upstream corner vortex at high chain extensibility is elucidated.

---

1. Introduction

Continuum level flow simulation of complex kinematics flows of dilute polymeric solutions has attracted considerable attention in the past two decades. However, in mixed kinematics flows continuum level and elastic dumbbell-based self-consistent multiscale flow simulations have not been able to quantitatively describe the experimentally observed flow dynamics, such as vortex growth, free surface and/or

† Email address for correspondence: bkhomami@utk.edu

interface motion, or the measured frictional drag properties to date (Talwar & Khomami 1992, Szabo, Rallison & Hinch 1997; Grillet *et al.* 1999; Yang & Khomami 1999; Al-Mubaiyedh, Sureshkumar & Khomami 2000; Li *et al.* 2000; Lee, Shaqfeh & Khomami 2002; Keunings 2004; Binding, Phillips & Phillips 2006). This lack of quantitative prediction of experimental findings can be attributed to the fact that elastic dumbbell-based closed form constitutive equations such as the FENE-P, FENE-CR and FENE-LS or micromechanical elastic dumbbell models can at best provide qualitative predictions of the macromolecular dynamics even in homogenous kinematics flows (Larson 2005; Shaqfeh 2005). However, mesoscopic level micromechanical descriptions, such as the bead-rod and bead-spring models with sufficient internal degrees of freedom have been found to predict both the dynamics of individual polymer molecules as well as the macroscopic rheological properties of dilute solutions with good accuracy, i.e. shear and extensional viscosity and first normal stress difference (Larson 2005; Shaqfeh 2005). These findings clearly underscore the necessity of multiscale simulations based on detailed mesoscopic level micromechanical models for quantitative prediction of the flow dynamics. This need has motivated development of a number of multiscale simulation techniques, namely, calculation of non-Newtonian flows: finite elements and stochastic simulation technique (CONNFFESSIT) (Laso & Öttinger 1993; Laso, Picasso & Öttinger 1997), Lagrangian particle method (LPM) (Halin *et al.* 1998) and Brownian configuration fields (BCF) (Hulsen, van Heel & van den Brule 1997; Öttinger, van den Brule & Hulsen 1997; Somasi & Khomami 2000, 2001). Although, the utility of these techniques in modelling dynamics of dilute polymeric solutions in a variety of complex kinematics benchmark flows (e.g. flow past a cylinder, sedimentation of spheres, etc) has been demonstrated, to date the micromechanical models used in this class of simulations have been very simplistic, i.e. the dilute solution has been modelled as a suspension of non-interacting single segment elastic dumbbells (e.g. Hua & Schieber 1998; Wapperom, Keunings & Legat 2000; Hu, Ding & Lee 2005; Bajaj *et al.* 2006; Philips & Smith 2006; Koppol, Sureshkumar & Khomami 2007).

Motivated by the superior predictive capability of bead-spring chain descriptions in homogenous kinematics flows, in this study we have pursued multiscale flow simulation of the 4:1:4 axisymmetric contraction and expansion flow, a long-standing benchmark complex kinematics flow problem, using bead-spring chain representation of the polymer molecules. Specifically, the micromechanical model parameters have been selected to closely match the measured rheological properties of a 0.025 wt % solution of a high molecular weight polystyrene (PS) dissolved in a low molecular weight polystyrene solvent (referred to as 0.025 wt % PS/PS Boger fluid). This choice of the flow geometry and the test fluid has been motivated by the fact that contraction expansion flows contain many essential flow features of typical polymer processing operations as well as the wealth of experimental data (Rothstein & McKinley 1999, 2001) on: (*a*) rheological properties of the test fluid, and (*b*) friction drag properties and vortex dynamics of the flow.

In addition to the aforementioned experimental studies by Rothstein & McKinley, many other investigators have focused their attention on measuring and predicting the frictional drag properties in this benchmark flow geometry as well as elucidating its vortex evolution pathways. Overall, the experimental studies (Cogswell 1972; Eisenbrand & Goddard 1982; Binding & Walters 1988; Boger & Binnington 1990, 1994; James & Chandler 1990; Cartalos & Piau 1992; Nigen & Walters 2002; Binding *et al.* 2006) have demonstrated that the dimensionless excess pressure drop (i.e. normalized with respect to its Newtonian flow counterpart) is close to unity at

small Deborah number (*De*, defined as the ratio of the fluid mean relaxation time to the characteristic deformation rate in the contraction tube) and at a critical flow rate corresponding to $De \cong 0.5$ it increases almost linearly until it reaches a plateau of approximately 3 at high flow rates ($De \cong 5$). In addition, at $De \cong 2.0$ a hydrodynamic instability is observed resulting in a transition from the two-dimensional axisymmetric steady flow to a three-dimensional time-dependent flow.

Rothstein & McKinley (1999, 2001, 2002) have hypothesized that the stress-conformation hysteresis (stress-conformation hysteresis behaviour arises due to distinct paths along which the polymer stress versus the polymer molecular conformation evolves during the stretching period in the contraction followed by the polymer relaxation downstream of the contraction) is responsible for the observed pressure drop enhancement for $De \leqslant 2.0$. Specifically, they conjectured that the coupling between the polymer stress and the flow kinematics during the distinct stretching and relaxation paths along the centreline of the flow geometry results in a net dissipation of energy leading to the enhancement of the pressure drop. However, the influence of stress-conformation hysteresis on friction drag properties of mixed kinematics flows has not been directly examined. This is mainly due to the fact that computational studies have generally failed to predict the experimentally observed pressure drop enhancement in many complex kinematics flows (Coates, Armstrng & Brown 1992; Keiller 1993; Oliveira *et al.* 2007). In fact to date, contraction/expansion flow simulations with closed form constitutive equations such as Oldroyd-B (Binding *et al.* 2006) and FENE-CR (Szabo *et al.* 1997) have generally predicted a reduction in the pressure drop with increasing *De*. The exceptions are computations with very low macromolecular finite extensibilities that have reported an initial decrease in the pressure drop followed by a very small increase of the order of 10 % (Szabo *et al.*).

The influence of fluid rheology on the vortex evolution pathways has also been extensively investigated. Overall, two predominant patterns are observed experimentally. These include, the growth of the upstream corner vortex (Coates *et al.* 1992; Purnode & Crochet 1996; Szabo *et al.* 1997; Rothstein & McKinley 1999, 2001) or the shrinkage of the upstream corner vortex coupled with formation and growth of a lip vortex (Lawler *et al.* 1986; Boger 1987; Boger & Binnington 1990, 1994; McKinley *et al.* 1991; Mompean & Deville 1997; Alves, Oliveira & Pinho 2004; Kim *et al.* 2005) that eventually merges with the upstream corner vortex.

This brief overview of the contraction/expansion flow of dilute polymeric solutions clearly highlights that even in the case of this long-standing benchmark flow problem, quantitative predictions of the frictional drag characteristics of dilute polymeric solutions have not been accomplished and more importantly the mechanism leading to the enhanced frictional resistance has not been established. To this end, results of a self-consistent multiscale flow simulation in a 4:1:4 axisymmetric contraction and expansion geometry is presented that for the first time provides a quantitative description of the enhanced pressure drop as a function of *De* in a 0.025 wt % PS/PS Boger fluid. In addition, based on an energy dissipation analysis the mechanism of the enhanced pressure drop observed in this class of flows is elucidated. Finally, we briefly discuss the influence of the macromolecular chain extensibility on the vortex dynamics.

2. Flow geometry

The 4:1:4 axisymmetric contraction and expansion flow geometry is schematically represented in figure 1(*a*). In this geometry the fluid flows from an upstream tube
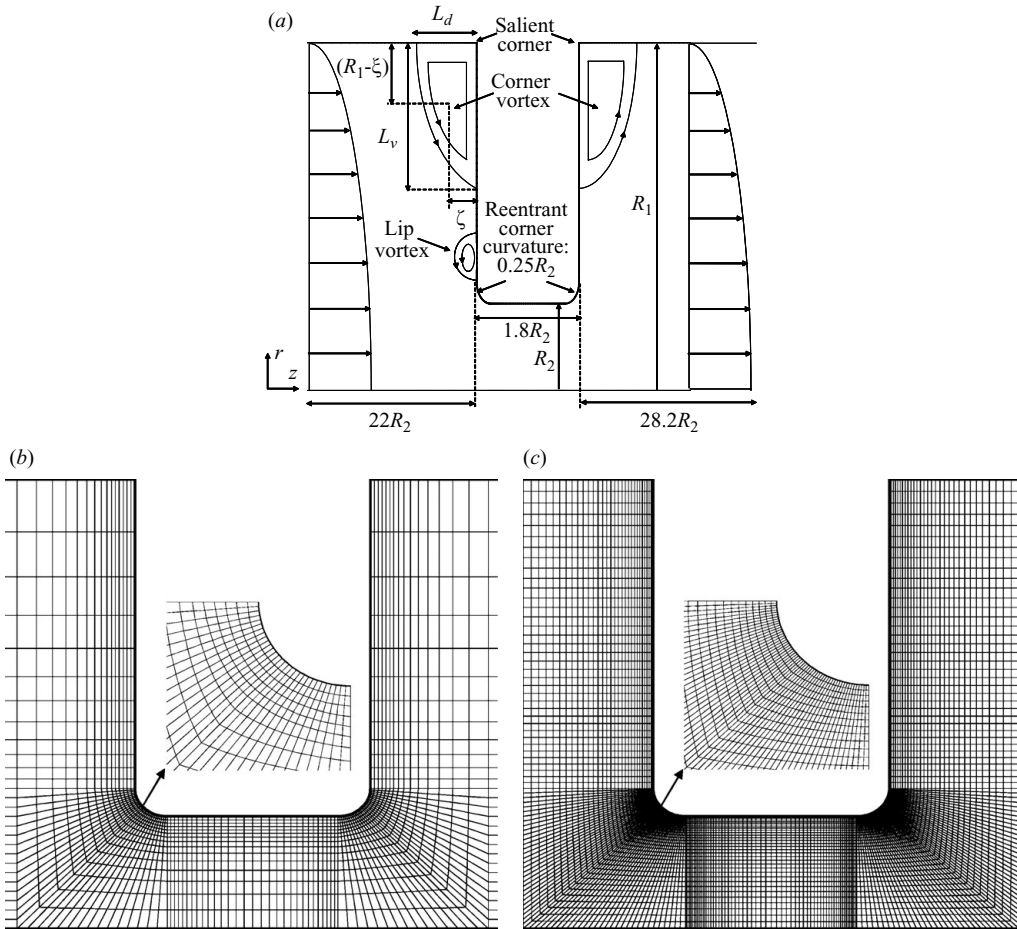
FIGURE 1. (*a*) Schematic diagram of the 4:1:4 axisymmetric contraction and expansion flow geometry; (*b*) 2736 elements mesh topology near the contraction expansion region; (*c*) 5476 elements mesh topology near the contraction expansion region.

of radius R_1 into a narrow contraction tube of radius R_2, and then back into a downstream tube of radius R_1. The contraction ratio, defined as R_1/R_2 and the contraction length (L_c/R_2) are set to 4 and 1.8, respectively, to match the experimental study of Rothstein & McKinley (1999, 2001). In addition, the upstream and downstream tubes of the flow geometry are chosen to be sufficiently long so that fully developed flow can be assumed at the entrance and exit.

In the presence of the sharp re-entrant corners, polymer stress singularities are observed in numerical simulations of viscoelastic fluids (Renardy 1997; Rallison & Hinch 2004). Motivated by the experimental flow geometry, rounded corners with the radius of curvature (R_c/R_2) of 0.25 have been chosen to avoid stress singularities. It should be noted that rounding of the re-entrant corner does not qualitatively alter the pressure drop enhancement and vortex characteristics, but it has been found to delay the onset of the aforementioned flow transition from two-dimensional steady to a three-dimensional time-dependent flow (Rothstein & McKinley 2001).

3. Problem formulation

3.1. *Governing equations*

The equations governing creeping isothermal flow of a dilute polymeric solution in the absence of body forces are as follows:

$$-\nabla P + \nabla \cdot \boldsymbol{\tau} = 0, \tag{1}$$

$$\nabla \cdot \boldsymbol{u} = 0, \tag{2}$$

where $\boldsymbol{u}$, the velocity vector is non-dimensionalized with respect to $u_{z,max}(z=0)$, which is the maximum velocity at the entrance of the flow geometry. The pressure P and the stress tensor $\boldsymbol{\tau}$ have been made dimensionless with respect to $\eta_o u_{z,max}(z=0)/R_2$ in which η_o is the fluid zero shear viscosity. The total stress $\boldsymbol{\tau}$ is split into a polymeric contribution $\boldsymbol{\tau}_p$ and a solvent contribution $\boldsymbol{\tau}_s$ (i.e. $\boldsymbol{\tau} = \boldsymbol{\tau}_p + \boldsymbol{\tau}_s$). The solvent is assumed to be a Newtonian fluid. Hence, $\boldsymbol{\tau}_s = 2\beta\dot{\boldsymbol{\gamma}}$, where $\dot{\boldsymbol{\gamma}} = \frac{1}{2}(\nabla\boldsymbol{u} + \nabla\boldsymbol{u}^T)$ is the rate of deformation tensor, $\beta = \eta_s/\eta_o$ and η_s is the solvent viscosity.

At the continuum level, the polymeric stress $\boldsymbol{\tau}_p$ is obtained by using the FENE-P constitutive equation (Bird *et al.* 1987):

$$\boldsymbol{\tau}_p + We(\boldsymbol{\tau}_p z)_{(1)} + (1 - \beta)(\boldsymbol{I}z)_{(1)} = 0, \tag{3}$$

where We is the Weissenberg number defined as $\lambda_m u_{z,max}(z=0)/R_2$ in which λ_m is the mean relaxation time of the polymer, and

$$z = 1 / \left(1 + \frac{3}{b} + \frac{We}{(1-\beta)b} \mathrm{Tr}(\boldsymbol{\tau}_p) \right), \tag{4}$$

where b is the maximum chain extensibility and Tr is the trace. The subscript (1) denotes the upper-convected derivative operator expressed as follows:

$$( )_{(1)} = \frac{\partial( )}{\partial t} + \boldsymbol{u} \cdot \nabla( ) - \boldsymbol{\kappa} \cdot ( ) - ( ) \cdot \boldsymbol{\kappa}^T, \tag{5}$$

where $\boldsymbol{k} = \nabla\boldsymbol{u}^T$.

When the polymer dynamics is described by a FENE dumbbell or a bead-spring chain, $\boldsymbol{\tau}_p$ is evaluated using the Kramers' expression (Bird *et al.* 1987):

$$\boldsymbol{\tau}_p = \frac{(1-\beta)}{We^*} \sum_{i=1}^{N} (\langle \boldsymbol{F}_i \boldsymbol{Q}_i \rangle - \langle \boldsymbol{F}_i \boldsymbol{Q}_i \rangle_{eqbm}), \tag{6}$$

where $We^* = We/(1 + 5/b)$ (Wiest & Tanner 1989), N is the number of segments in the bead-spring chain, $bs = NHQ_0^2/k_BT$, Q_0 is the maximum extensibility of each segment, H is the spring constant, $\boldsymbol{Q}_i$ is the segmental connectivity vector which is non-dimensionalized with respect to its equilibrium length $\sqrt{k_BT/H}$, $\langle \cdot \rangle$ denotes the ensemble average, $\langle \boldsymbol{F}_i \boldsymbol{Q}_i \rangle_{eqbm} = \boldsymbol{I}$ (the unit tensor) and $\boldsymbol{F}_i$ is the nonlinear FENE force law for the ith segment given by

$$\boldsymbol{F}_i = \frac{\boldsymbol{Q}_i}{1 - \left(NQ_i^2/bs \right)}. \tag{7}$$

The temporal evolution of the segmental connectivity vector $\boldsymbol{Q}_i$ of the ith segment of the FENE bead-spring model under flow is determined using the Brownian configuration field (BCF) approach (Hulsen *et al.* 1997; Somasi & Khomami 2000) since it is ideally suitable for implementation in the finite element context. The BCF

evolution equation for the segmental connectivity is given as

$$d\mathbf{Q}_i(x,t) = \left[-\mathbf{u}(x,t)\cdot\nabla\mathbf{Q}_i(x,t) + \mathbf{\kappa}(x,t)\cdot\mathbf{Q}_i(x,t) + \frac{\mathbf{F}_i^E}{4We}\right]dt$$

$$+ \sqrt{\frac{1}{2We}}[d\,\mathbf{W}_{i+1}(t) - d\,\mathbf{W}_i(t)], \quad (8)$$

where

$$\mathbf{F}_i^E = \begin{cases} -2\mathbf{F}_i + \mathbf{F}_{i+1}; & i = 1, \\ \mathbf{F}_{i-1} - 2\mathbf{F}_i + \mathbf{F}_{i+1}; & 1 < i < N, \\ \mathbf{F}_{i-1} - 2\mathbf{F}_i; & i = N. \end{cases} \quad (9)$$

The last term in (8) accounts for the Brownian force experienced by the ith bead, which is characterized by the Wiener process ($d\mathbf{W}_i(t)$) which is mathematically represented as a Gaussian random vector with a zero mean and a dt variance.

3.2. *Computational technique*

The discrete elastic viscous stress splitting (DEVSS-G) finite element formulation (Guenette & Fortin, 1995; Li *et al.* 1998) is used to discretize the momentum and mass conservation equations. The weak forms of these equations are obtained using the Galerkin procedure:

$$[(\nabla\mathbf{v}) : (\nabla\mathbf{u} + \nabla\mathbf{u}^T - P\mathbf{I} + \mathbf{\tau}_p - (1-\beta)(\mathbf{G} + \mathbf{G}^T))] = [\mathbf{v} : \mathbf{\sigma}]_\Gamma, \quad (10)$$

$$[q \; ; \; \nabla\cdot\mathbf{u}] = 0, \quad (11)$$

$$[g : (\mathbf{G} - \nabla\mathbf{u})] = 0. \quad (12)$$

In the above equations $\mathbf{G}$ is the discrete interpolant for the velocity gradient ($\nabla\mathbf{u}$). $[a : b]$, $[a; b]$ and $[a : b]_\Gamma$ are the standard inner products of (a, b) in the flow domain Ω and on the boundary Γ, respectively. Here σ is the traction vector on the boundary.

Hierarchic shape functions based on the Legendre polynomials (Szabo & Babuska 1987; Somasi & Khomami 2000) are used to approximate the variables within the quadrilateral finite elements used to discretize the flow domain Ω. Specifically, in accordance with the Brezzi–Babuska condition (Khomami *et al.* 1994) second-order polynomials ($p = 2$) are used to approximate the velocity components, while bilinear shape functions ($p = 1$) are used for the velocity gradient and pressure variables. Moreover, similar to our earlier studies (Talwar, Ganpule & Khomami 1994; Somasi & Khomami 2000) bilinear shape functions ($p = 1$) are used to approximate the stress variables.

The FENE-P closed form constitutive equation and the segmental connectivity vector equation are discretized using the SUPG technique function where the Galerkin weight function $\mathbf{\phi}$ is modified as follows, $\mathbf{Y} = \mathbf{\phi} + (\mathbf{u}\cdot\nabla\mathbf{\phi})h/|\mathbf{u}|$, with h being the characteristic element length (Brooks & Hughes 1982; Smith *et al.* 2000; Somasi & Khomami 2000). This results in the following set of equations:

$$[(\mathbf{\tau}_p + We(\mathbf{\tau}_p z)_{(1)} + (1-\beta)(\mathbf{I}z)_{(1)}) : \mathbf{Y}] = 0, \quad (13)$$

$$[(d\mathbf{Q}_i - \left(-\mathbf{u}\cdot\nabla\mathbf{Q}_i + \mathbf{\kappa}\cdot\mathbf{Q}_i + \frac{1}{4We}\mathbf{F}_i^E\right)dt - \sqrt{\frac{1}{2We}}(d\mathbf{W}_{i+1}(t) - d\mathbf{W}_i(t))) : \mathbf{Y}] = 0,$$

$$(14)$$

where $\mathbf{Y}$ is selected from the bilinear continuous polynomial space ($p = 1$).

Mesh characteristic	2736 Element mesh	5476 Element mesh
Number of nodes	2904	5711
Number of sides	5639	11186
Min. characteristic length	0.0227	0.0209

TABLE 1. Domain discretization details.

Variable(s)	DOF: 2736 Element mesh	DOF: 5476 Element mesh
$\boldsymbol{u}$	11 279	22 373
P	2904	5711
$\boldsymbol{G}$ and $\boldsymbol{\tau}$	11 616	22 844
$\boldsymbol{Q}$ when $N = 1$ and $N_f = 1024$	8 921 088	17 544 192
$\boldsymbol{Q}$ when $N = 3$ and $N_f = 960$	25 090 560	49 343 040

TABLE 2. Degrees of freedom (DOF) for each variable.

For the FENE dumbbell or the bead-spring chain, $\boldsymbol{\tau}_p$ is evaluated using the Kramers' expression via Galerkin projection:

$$\left[\left(\boldsymbol{\tau}_p - \frac{(1-\beta)}{We^*} \sum_{i=1}^{N} (\langle \boldsymbol{F}_i \, \boldsymbol{Q}_i \rangle - \boldsymbol{I}) \right) : \boldsymbol{a} \right] = 0, \qquad (15)$$

where $\boldsymbol{a}$ is chosen from the bilinear continuous polynomial space ($p = 1$).

3.3. *Boundary conditions*

The boundary conditions are the standard no slip boundary condition ($u_r = u_z = 0$) along the wall, symmetry boundary condition ($u_r = 0$, $\partial u_z / \partial r = 0$) along the centreline ($r = 0$), fully developed unidirectional velocity profile and stresses are enforced at the entrance and exit. The reference value for P is set to zero at the exit, and the value of the pressure at the entrance, which is a function of We is computed.

3.4. *Domain discretization*

The flow domain has been divided into structured finite element meshes consisting of quadrilateral elements. Two meshes of sizes 2736 and 5476 elements based on the same topology have been used to simulate the flow. This level of mesh refinement has been shown to provide accurate solutions in prior continuum level simulations with the FENE-CR constitutive equation (Szabo *et al.* 1997). The magnified mesh configurations near the contraction are shown in figures 1(*b*) and 1(*c*). Details of the principal characteristics of each mesh are presented in table 1, and the degrees of freedom corresponding to each of the variables are given in table 2.

3.5. *Computational details*

The FENE dumbbell and bead-spring self-consistent multiscale contraction/ expansion flow simulations have been performed using our recently developed, highly efficient, parallel multiscale simulation algorithm (Koppol *et al.* 2007). In these simulations a time step $\Delta t = 10^{-3}$ and a tolerance $\varepsilon = 10^{-3}$ for convergence within each time step has been employed. The number of configuration fields N_f used for the FENE dumbbell and FENE chain simulations were 1024 and 960, respectively. The FENE-P computations were performed using the semi-implicit predictor-corrector scheme described in detail in Koppol (2007) with $\Delta t = 10^{-3}$ and

Model	2736 Element mesh	5476 Element mesh
3seg FENE $b_{max} = 225$	$De = 0.043, 0.087, 0.130, 0.217,$ $0.304, 0.372, 0.45, 0.5$	–
FENE-P $b_{max} = 300$	$De = 0.043, 0.087, 0.130, 0.173,$ 0.217	$De = 0.260, 0.303, 0.390, 0.477, 0.520,$ $0.542, 0.563, 0.585, 0.607$
1seg FENE $b_{max} = 1800$	$De = 0.043, 0.217, 0.347, 0.520,$ $0.650, 0.813$	$De = 0.915, 1.018, 1.232, 1.326, 1.506$
3seg FENE $b_{max} = 4500$	$De = 0.043, 0.130, 0.217, 0.303,$ $0.450, 0.650$	$De = 0.813, 0.915, 1.018, 1.232, 1.326$

TABLE 3. Details of finite element meshes used for computations with specific models at various *De*.

$\varepsilon = 10^{-3}$. To accelerate convergence first-order continuation in We was utilized. To enhance the accuracy of the mean and reduce the standard deviation of the results of the self-consistent multiscale simulation, steady state results have been obtained by averaging the statistically stationary results of at least 3000 time steps.

Rothstein & McKinley (1999, 2001) have reported their experimental results as a function of the Deborah number $De = \lambda_0 \langle u_z \rangle_2 / (R_2 + R_c)$ defined based on the characteristic zero shear relaxation time of the fluid (λ_0) and the characteristic deformation rate in the contraction with rounded re-entrant corners, $\langle u_z \rangle_2 / (R_2 + R_c)$, where $\langle u_z \rangle_2$ is the average velocity in the contraction. To facilitate comparison with the experimental data, the simulation results are reported in terms of De ($We \sim 2.5\,De$). Table 3 summarizes the mesh size used for all the FENE computations. As noted earlier, the meshes used in this study have been shown to provide accurate solutions in prior continuum level simulations with the FENE-CR constitutive equation. To this end, we have adopted a simple strategy in our computations, namely, the 2736 element mesh has been employed in the simulations up to De for which its solution was found to be accurate. Higher De simulations were pursued with the 5476 element only when interesting alterations in the vortex dynamics or the pressure drop enhancement were anticipated. All the simulation results presented in this paper have been verified for convergence (see §5.1).

4. Fluid rheology

Figure 2 depicts the experimentally measured steady shear viscosity (η) and first normal stress coefficient (Ψ_1) as a function of the shear rate ($\dot{\gamma}$). The solvent viscosity, η_s, the zero shear viscosity η_0 and the zero shear first normal stress difference, Ψ_{10}, at $25°$ C are 21.0, 22.75 Pa.s and 6.66 Pa.s^2, respectively. The ratio of the solvent viscosity to fluid zero shear viscosity is defined as $\beta = \eta_s / \eta_0 = 0.92$.

In addition, the small amplitude oscillatory shear flow properties, i.e. the dynamic viscosity (η') and rigidity (η''/ω) versus the frequency of oscillation (ω), as well as the transient extensional viscosity (η^E) at various strain rates ($\dot{\varepsilon}$) (Rothstein & McKinley 1999, 2001) is also shown in figure 2. Various models, namely, FENE bead-spring chains, FENE dumbbell and the FENE-P closed form constitutive equation have been used to describe the rheological behaviour of the 0.025 wt % PS/PS Boger fluid. Linear viscoelastic fits for η' and η''/ω demonstrate that two modes are essentially required to quantitatively describe the small amplitude oscillatory shear flow behaviour of the polymer molecules (see table 4, the third mode has a very small relaxation time, hence

Mode (i)	η_i (Pa.s)	λ_i (s)
1	1.0695	2.8742
2	0.3509	0.1312
3	0.000255	21.33

$$\lambda_m = \sum_{i=1}^{2} \eta_i \lambda_i / \sum_{i=1}^{2} \eta_i = 2.197$$

TABLE 4. Linear viscoelastic properties of the 0.025 wt % PS/PS Boger fluid at 25° C.
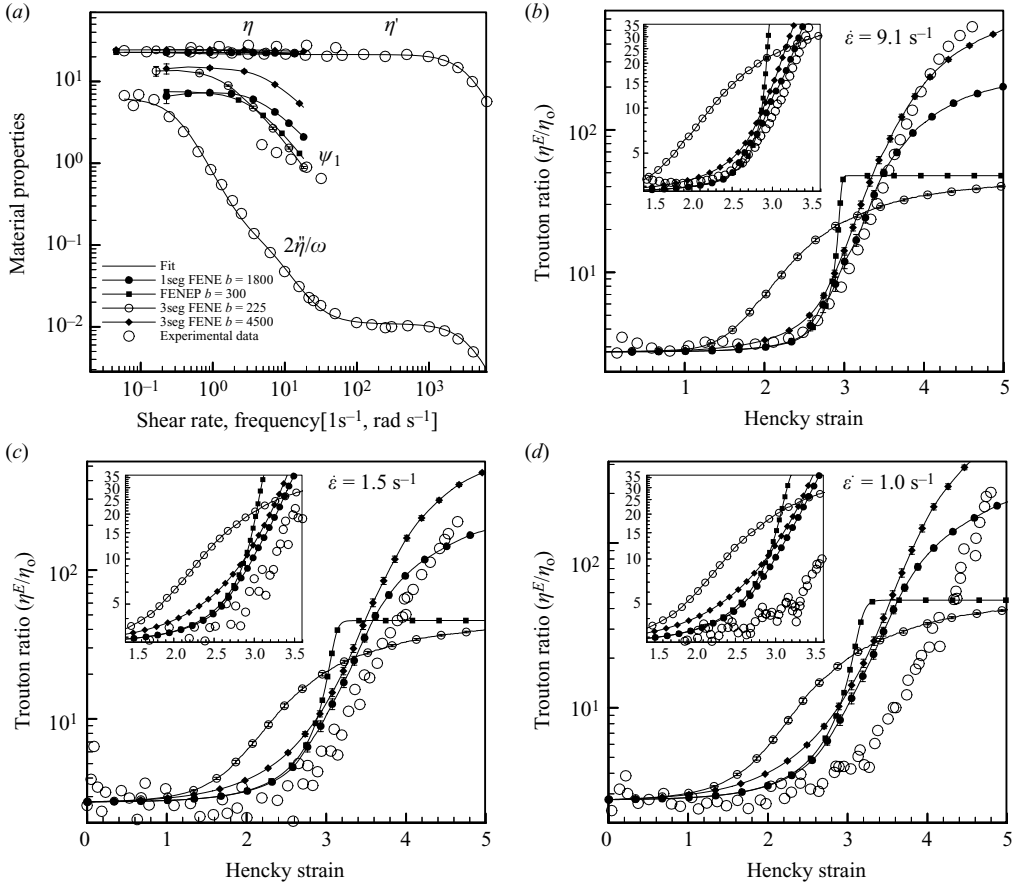
FIGURE 2. Rheological characterization of the 0.025 wt % PS/PS Boger fluid at 25° C (*a*) η versus $\dot{\gamma}$, Ψ_1 versus $\dot{\gamma}$, η' versus ω, and η''/ω versus ω; (*b*) η^E/η_0 versus ε at $\dot{\varepsilon} = 9.1$ s^{-1}; (*c*) η^E/η_0 versus ε at $\dot{\varepsilon} = 1.5$ s^{-1}; (*d*) η^E/η_0 versus ε at $\dot{\varepsilon} = 1$s^{-1}.

its contribution has been combined with the solvent). The mean relaxation time of the polymer molecule (λ_m) based on this two mode description is found to be 2.197 s.

To determine the model time constant λ_H for the FENE dumbbell and the FENE-P constitutive equation a proven technique, namely matching of the mean relaxation time of the solution λ_m to the characteristic zero shear relaxation time ($\Psi_{10}/2\eta_{p0}$) of the model has been adopted (Somasi *et al.* 2002). In the case of the FENE bead-spring chains, λ_H has been evaluated using the following expression derived by Weist &

Model	η_0	ψ_{10}
3seg FENE $b_{max} = 225$	24.333 ± 0.095	13.604 ± 0.593
FENE-P $b_{max} = 300$	22.729	7.439
1seg FENE $b_{max} = 1800$	22.658 ± 0.107	7.140 ± 0.533
3seg FENE $b_{max} = 4500$	24.369 ± 0.233	14.630 ± 0.637

TABLE 5. Zero shear properties, η_0 and Ψ_{10} predicted by different polymer models.

Tanner (1989):

$$\lambda_H = \frac{\lambda_m}{d}, \text{ where } d = \left(\frac{b+7}{15N}\right)\left(\frac{1}{b/N+5}\right)\left((2(N+1)^2+7) - \frac{12((N+1)^2+1)}{(N+1)(b/N+7)}\right).$$

(16)

In the above expression the maximum chain extensibility, b of the FENE and FENE-P models has been selected in order to reproduce closely the steady shear and the transient extensional rheology of the fluid. It should be noted that the rheological predictions of the FENE-based models have been obtained via Brownian dynamics simulations using a semi-implicit predictor-corrector scheme (Somasi *et al.* 2002) with the ensemble size $N_t = 1024$, while those of the FENE-P closed form constitutive model has been obtained using the semi-implicit predictor-corrector scheme described in detail in Koppol (2007). The time step Δt for performing the time integration in both of the semi-implicit predictor-corrector schemes has been chosen to be 10^{-3}. Also shown in figure 2 are the statistical errors of the computed quantities ($\sqrt{\sigma^2/N_t}$, where σ^2 is the variance of the quantity of interest).

Figure 2(*a*) summarizes the variation of η and Ψ_1 versus $\dot{\gamma}$ evaluated using the FENE and FENE-P models with different b values. As expected, the FENE and FENE-P models estimate the slight shear thinning of the fluid viscosity with reasonable accuracy; however, models with lower b (i.e. 225 and 300) predict Ψ_1 values that are closer to the experimental value as compared to models with higher b values. However, it should be noted that the predictions of FENE models with $b = 1800$ and 4500 evidently will provide a good description of Ψ_1 at higher $\dot{\gamma}$ values for which accurate experimental data is not available. Table 5 provides the predicted zero shear properties by all the models.

The transient response of the FENE and FENE-P models with different b values to a steady uniaxial extensional flow at different extension rates quantified in terms of $\eta^E = 3\eta_s + \eta_p^E$, where η_p^E is the extensional viscosity contribution from the polymer molecules is shown in figures 2(*b*), 2(*c*) and 2(*d*). As expected, for $\varepsilon < 1.5$ the Trouton ratio (η^E/η_0) for both the FENE and FENE-P models is nearly 3.0. Moreover, the strain hardening sets in for values of ε between 1.5 and 3.5. The insets in figures 2(*b*), 2(*c*) and 2(*d*) show the strain hardening behaviour of the FENE and FENE-P models. Specifically, the FENE model with $b = 225$ and the FENE-P models with $b = 300$ demonstrate strain hardening at lower values of ε compared to the experimental measurements. Whereas the one segment FENE model with $b = 1800$ and the three segment FENE model with $b = 4500$ predict the strain hardening at ε values similar to those in the experiments, particularly at the higher strain rate, namely, $\dot{\varepsilon} = 9.1 \text{ s}^{-1}$. Moreover, for ε above 3.5, η^E predicted by the FENE model with $b = 225$ and the FENE-P model with $b = 300$ approach their steady state values, whereas η^E for all the models with higher b continues to increase in accordance with the experimental data.

Also, for values of $\varepsilon > 3.5$ the three segment FENE model with $b = 4500$ faithfully reproduce the experimental measurement at $\dot{\varepsilon} = 9.1 \text{ s}^{-1}$, while the one segment FENE model with $b = 1800$ somewhat under predicts η^E at this extension rate.

Overall, all the FENE and FENE-P models considered provide relatively similar predictions for the steady shear properties (η and Ψ_1). However, only the one segment FENE model with $b = 1800$ and the three segment FENE model with $b = 4500$ provide a reasonably good prediction of η^E particularly in the experimental strain range of interest, i.e. from 2.5 to 4, at $De \sim O(1)$, where significant excess pressure drop enhancement is observed experimentally.

5. Results and discussion

5.1. *Solution accuracy*

As mentioned earlier, the domain discretizations used in this study have been shown to provide accurate solutions in prior continuum level simulations with the FENE-CR constitutive equation (Szabo *et al.* 1997). To demonstrate the accuracy of the self-consistent multiscale simulations, the self-consistent stress profiles have compared with those obtained based on a Lagrangian Brownian Dynamics (BD) technique. This approach for establishing the solution accuracy has been adopted since the conventional way of comparing solutions from multiple meshes is highly computationally intensive in the case of the multiscale simulations evident from the large number of degrees of freedom at each time step (table 2). Specifically, the comparisons are made based on the $\tau_{p,zz}$ component of the polymeric stress because of its large variation in the contraction/expansion region and with De as well as its significant influence on the excess pressure drop enhancement.

The Lagrangian determination of the stress involves two steps. First, particle paths are determined via integration of the local self-consistent velocity vector ($\boldsymbol{u}$) using the fourth-order Runge–Kutta method. In turn, BD simulations are conducted along selected streamlines utilizing the semi-implicit predictor scheme of Somasi *et al.* (2002) with the ensemble size $N_t = 1024$. The integrations are carried out by varying Δt such that the magnitude of $\boldsymbol{u} \, \Delta t$ is fixed to a constant, $2 \times 10^{-2} \geqslant A \geqslant 4 \times 10^{-4}$. Specifically, the constant is set to A when $z \in [19, 25]$, $5A$ when $z \in [16, 19)$ and $(25, 32]$, and $25A$ when $z \in [0, 16)$ and $(32, 52]$. With $A \geqslant 1 \times 10^{-4}$, converged results in the De range of interest are obtained. At this level of refinement, highly spatially resolved polymer stresses are obtained. Hence, the computed stresses utilizing this Lagrangian procedure should provide a very stringent test of the self-consistent computed stresses.

Figure 3 depicts comparison of prototypical steady state $\tau_{p,zz}$ profiles along streamlines near the wall and centreline of the channel in the vicinity of the contraction at various De and finite chain extensibility. Overall, the excellent agreement between the self-consistent simulations and the Lagrangian-based results clearly demonstrate the accuracy of the self-consistent multiscale simulation results.

5.2. *Pressure drop enhancement*

To make a one-to-one comparison with the experimental data, the model predictions will be presented in terms of the dimensionless pressure drop $\tilde{P}$ which is defined as the ratio of the extra pressure drop for the non-Newtonian flow ($De > 0$) through the geometry with a prescribed re-entrant corner curvature to that of the Newtonian flow ($De = 0$) at the same flow rate with sharp re-entrant corners:

$$\tilde{P} = \frac{\Delta P_{Ex}(De \geqslant 0, R_c)}{\Delta P_{Ex}(De = 0, R_c = 0)}. \tag{17}$$
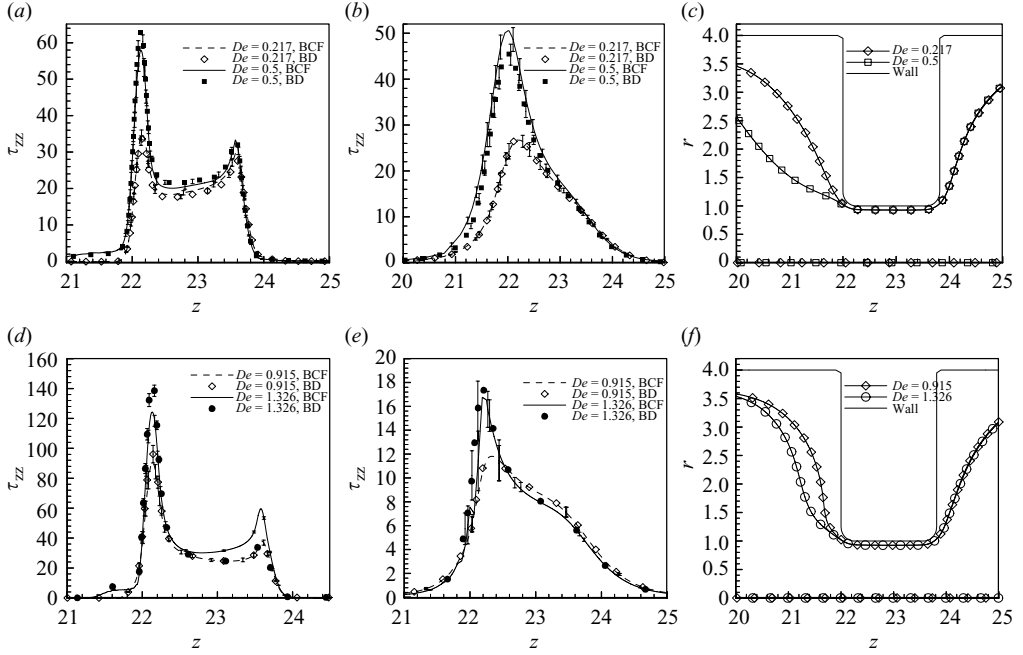
FIGURE 3. Representative stress profiles ($\tau_{p,zz}$). Three segment bead-spring chain with $b = 225$ along streamlines originating form (*a*) $(0, 3.7)$ and (*b*) $(0, 0)$ whose paths are shown in (*c*). FENE dumbbell with $b = 1800$ along streamlines originating form (*d*) $(0, 3.7)$ and (*e*) $(0, 0)$ whose paths are shown in (*f*).

With this definition, the extra pressure drop ΔP_{Ex} is then solely due polymer modification of the pressure drop in the contraction and expansion flow alone, since the pressure drop caused due to the Poiseuille flow in the straight upstream ($\Delta P_{up} = 5.5$), downstream ($\Delta P_{down} = 7.05$) and contraction ($\Delta P_{con} = 115.2$) tubes have been subtracted from the total pressure drop across the flow geometry (ΔP). Rothstein & McKinley (1999, 2001) have approximated the extra pressure drop for the Newtonian flow $\Delta P_{Ex}(De = 0, R_c = 0))$ utilizing Sampson's solution for the pressure drop across the orifice with sharp corners in an infinite rigid wall (Happel & Brenner 1965). This value when corrected for an orifice with finite aspect ration and scaled with $\eta_o u_{z,max}(z = 0)/R_2$ is 75.4. The available experimental measurements for $\tilde{P}$, however, are for the flow geometry that contains a rounded re-entrant corner. Hence, $\tilde{P}$ has been shifted using the procedure outlined by Rothstein & McKinley (2001):

$$\tilde{P}_{shift}(De) = \tilde{P}(De) + C_s, \tag{18}$$

where C_s is defined as $C_{s(\beta, R_c)} = P_{sharp}(De = 0) - P_{curved}(De = 0)$. This Couette-like correction term is used to take into account the pressure observed in the Newtonian flow through the curved entrance region. Figure 4 depicts the evolution of the shifted dimensionless pressure drop $\tilde{P}_{shift}$ with De. It should be noted that at $De \approx 0$, $\tilde{P}_{shift}$, for the one segment FENE and FENE-P models, approaches the expected value of 1. However, for the three segment FENE models, ΔP has to be scaled (at all De) with $\eta_0^{3seg} u_{z,max}(z = 0)/R_2$ instead of $\eta_o u_{z,max}(z = 0)/R_2$ before computing $\tilde{P}$ and shifting it (η_0^{3seg} corresponds to the fluid zero shear viscosity predicted by three segment FENE
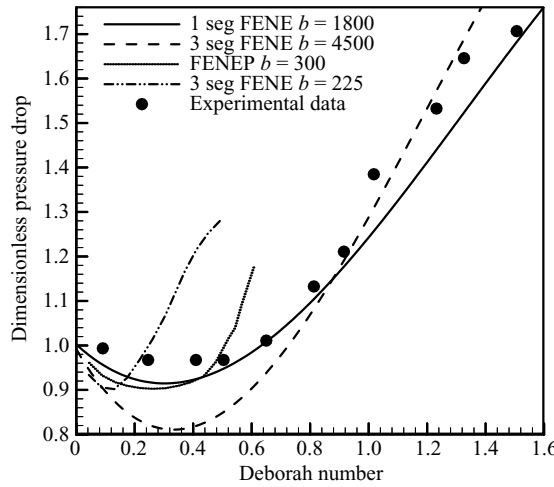
FIGURE 4. Dimensionless excess pressure drop ($\tilde{P}_{shift}$) as a function of De.

models). This demonstrates the importance of matching the model estimated zero shear viscosity with that of the fluid (η_0) to capture the experimentally observed pressure drop in the limit of $De \rightarrow 0$.

As De is enhanced, the computed $\tilde{P}_{shift}$ for all the models pass through a minimum after which they increase monotonically to a value well above that of the Newtonian flow. Also as the chain maximum extensibility is enhanced the minimum value reached decreases. This observation is consistent with the earlier computations with the FENE-CR (Szabo *et al.* 1997) and Oldroyd-B (Binding *et al.* 2006) constitutive models. Furthermore, as the chain extensibility increases, the onset of growth of $\tilde{P}_{shift}$ occurs at a higher De in a very similar manner as the onset of the strain hardening of the transient extensional viscosity (η^E) at higher Hencky strains. Hence, both FENE and FENE-P models with low chain finite extensibility highly over predict the experimentally measured excess pressure drop enhancement, while, the FENE models with high finite extensibility that can faithfully capture the experimentally measured η^E at high strain rates, provide a reasonable good prediction of the excess pressure drop enhancement. In particular, the three segment FENE chain with maximum extensibility of 4500 accurately predicts the measured pressure drop enhancement at $De \sim O(1)$.

5.3. Energy dissipation analysis

In the above discussion, it has been suggested that the predicted excess pressure drop as a function of De is closely correlated with the strain hardening character of the fluid. In order to ascertain the relationship between the excess pressure drop and the extensional characteristics of the test fluid, we have carried out an energy dissipation analysis. It is well known that the rate of stress work ($\dot{W}$) within an arbitrary control volume (V), in the absence of body forces, can be expressed in terms of the integral over its surface (S) as:

$$\dot{W} = \int_S \boldsymbol{u} \cdot \pi \cdot \hat{n} \, \mathrm{d}S, \tag{19}$$

where $\boldsymbol{u}$ is the local fluid velocity, $\pi = -P\boldsymbol{I} + \boldsymbol{\tau}_s + \boldsymbol{\tau}_p$ is the total stress on the surface element $\mathrm{d}S$ with a unit outward normal $\hat{n}$. Moreover, for creeping flows ($\nabla \cdot \pi = 0$) the
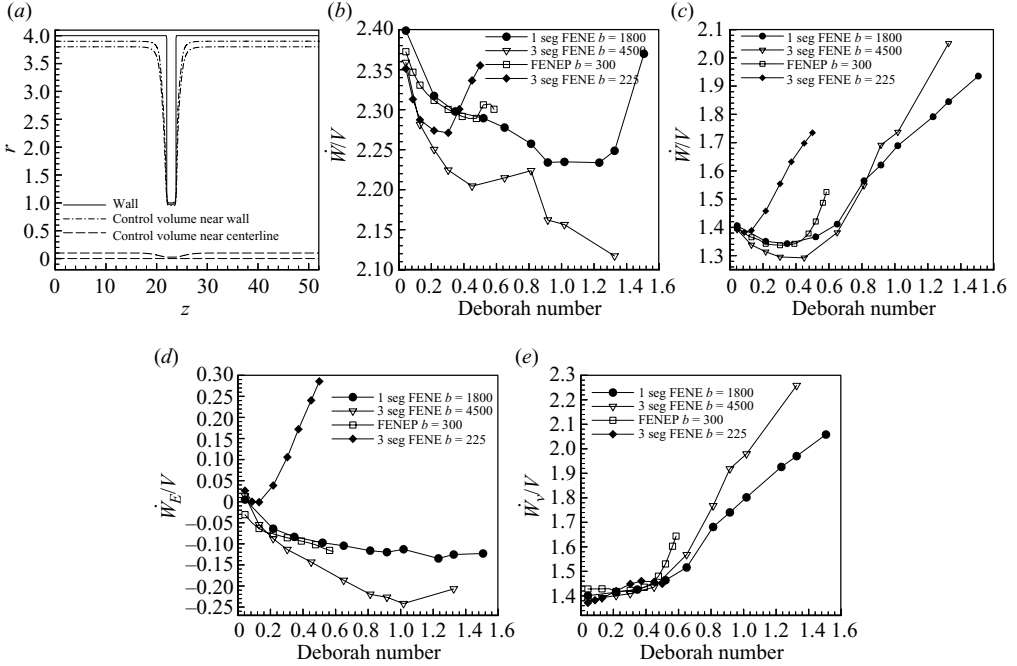
FIGURE 5. (*a*) Control volumes selected for the computation of the rate of stress work; (*b*) normalized stress work in the near wall region; (*c*) normalized stress work in the centreline region; (*d*) rate of elastic stress work ($\dot{W}_E$) in the centreline region; (*e*) rate of viscous stress work ($\dot{W}_V$) stress work in the centreline region.

surface integral in (19) can be simplified to a volume integral:

$$\dot{W} = \int_V \pi : \nabla \boldsymbol{u} \, \mathrm{d}V. \tag{20}$$

Since the flow under consideration is periodic and $\boldsymbol{u} = 0$ along the stationary walls, equation (19) reduces to a simple relation between the rate of stress work in the entire flow domain ($\dot{W}_{tot}$) and the pressure drop across the flow geometry ΔP, i.e. $\dot{W}_{tot} = Q\Delta P$. Evidently, since ΔP is positive $\dot{W}_{tot}$ is always dissipative. Moreover, because of the direct relation between $\dot{W}_{tot}$ and ΔP, evaluation of the rate of stress work in a selected control volume within the flow domain provides a direct measure of ΔP in the control volume. Hence, we have selected to evaluate the stress work in two axisymmetric control volumes, one near the centreline (CV_1) and the other near the wall (CV_2) (see figure 5a). The choice of these two control volumes has been motivated by the fact that the polymeric stresses and their gradients are large in these two domains, moreover, the flow in CV_1 is mainly extensional, while the flow in CV_2 is dominated by shearing forces.

Figures 5(*b*) and 5(*c*) depict the variation of $\dot{W}$ as a function of *De*. As expected, $\dot{W}$ is positive in both control volumes indicating energy dissipation at all *De*. Moreover, as *De* is enhanced $\dot{W}$ reduces to a minimum value and then generally increases. The *De* at which the minimum in $\dot{W}$ is observed in CV_1 is approximately the same as the *De* where the minimum in the excess pressure drop is observed (see figure 4), while in CV_2 this minimum occurs at much higher *De*. More importantly, as *De* is

enhanced, $\dot{W}$ for all the models shows a significant increase above their Newtonian value in CV_1, while in CV_2 they always remain below the Newtonian value at least in the De range of our simulations. Overall, for all the models the enhancement of $\dot{W}$ with increasing De number in CV_1 is similar to that of the excess pressure drop enhancement (see figure 4). This is clearly not the case in CV_2. Hence, one can conclude that the excess pressure drop enhancement is controlled predominantly by the extensional flow near the centreline in the vicinity of the contraction and expansion region.

To further examine the mechanism that gives rise to the excess pressure drop enhancement in the extensional dominated region of the flow, we have divided the total stress tensor (π) into an elastic stress component due to the polymer ($\boldsymbol{\Sigma}$), a viscous polymer stress ($\boldsymbol{\tau}_{pv}$) and a solvent stress ($\boldsymbol{\tau}_s$), as well as the isotropic pressure ($-P\boldsymbol{I}$). Specifically, $\boldsymbol{\Sigma}$ can be obtained from the polymer stress ($\boldsymbol{\tau}_p$) by eliminating the polymer viscous stress ($\boldsymbol{\tau}_{pv}$) arising from the fast relaxing modes, which is approximated to be $2(1-\beta)\dot{\boldsymbol{\gamma}}$. In turn, the sum of the viscous stresses due to the polymer and the solvent ($\boldsymbol{\tau}_{pv} + \boldsymbol{\tau}_s$) is equal to $2\dot{\boldsymbol{\gamma}}$. For an incompressible flow the isotropic pressure does not contribute to $\dot{W}$, hence, the only contributions arise from the rate of the elastic stress work ($\dot{W}_E$) and the rate of viscous stress work ($\dot{W}_V$), i.e. $\dot{W} = \dot{W}_E + \dot{W}_V$, where:

$$\dot{W}_E = \int_V \boldsymbol{\Sigma} : \nabla \boldsymbol{u} \, \mathrm{d}V \text{ and } \dot{W}_V = \int_V (\boldsymbol{\tau}_{pv} + \boldsymbol{\tau}_s) : \nabla \boldsymbol{u} \, \mathrm{d}V. \tag{21}$$

Figures 5(d) and 5(e) show the variation of the rate of elastic and viscous stress works versus De in CV_1. In the limit of low finite extensibility, the FENE bead-spring chain shows a decrease in $\dot{W}_E$ at low De followed by a significant monotonic increase, however, the variation of $\dot{W}_V$ as a function of De for this model is not very significant. For all other models at low De (approximately less than 0.5) $\dot{W}_E$ quickly decreases while $\dot{W}_V$ slightly grows. However at high De, $\dot{W}_E$ asymptotes to a negative value while $\dot{W}_V$ continues to increase monotonically. The negative value of $\dot{W}_E$ clearly shows that the interaction between the polymeric elastic stress ($\boldsymbol{\Sigma}$) and the fluid kinematics ($\nabla \boldsymbol{u}$) results in energy recovery that manifests itself as reduction of the excess pressure drop at low De (see figure 4).

Overall, from this analysis it can be concluded that at low finite extensibility, the excess pressure drop enhancement as a function of De is occurring mainly due to the enhancement of elastic stress work, $\dot{W}_E$. On the other hand, at high finite extensibility the pressure drop enhancement as a function of De is mainly caused by the enhancement of $\dot{W}_V$ resulting from the polymer induced flow modification near the centreline.

5.4. *Role of the stress conformation hysteresis*

As mentioned earlier, Rothstein & McKinley (1999, 2001) have conjectured that the stress-conformation hysteresis observed in the contraction and expansion flow results in a net dissipation of energy leading to the enhancement of the excess pressure drop. Specifically they have indicated that a strong correlation exists between the area enclosed by the hysteresis loop along the centreline of the contraction and expansion flow and the excess pressure drop enhancement. To ascertain the validity of this hypothesis, we have examined the stress-conformation hysteresis observed along the centreline of the contraction and expansion flow. To this end, $\boldsymbol{\tau}_{p,zz}$ which is the dominant polymer stress component along the centreline as a function of
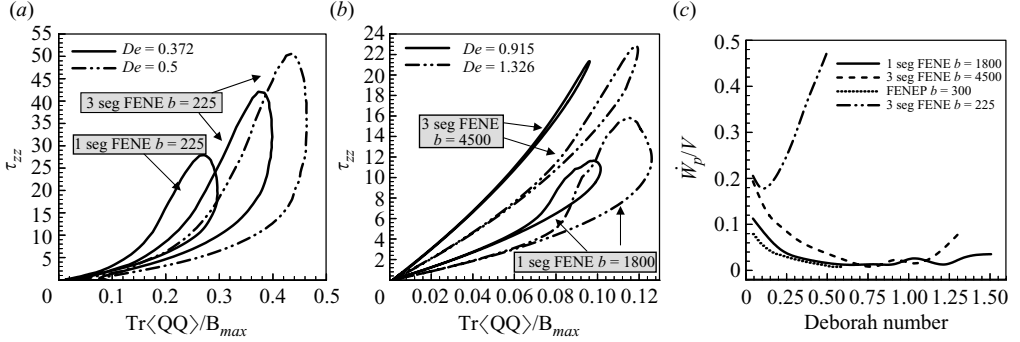
FIGURE 6. Stress conformation hysteresis along the centreline of the contraction expansion flow. (*a*) low *b* FENE models; (*b*) high *b* FENE models; (*c*) rate of polymer stress work versus *De*.

the ensemble average of the normalized trace of the conformation tensor $\langle \boldsymbol{QQ} \rangle$ at representative *De* are shown in figure 6. As expected, the hysteresis loops at lower finite extensibility for at low *b* are significantly larger than those at higher finite extensibility due to the fact that at a fixed *De* the maximum value of the normalized extension, i.e. the trace of $\langle \boldsymbol{QQ} \rangle /b$ is much higher at low b leading to significant nonlinearity of the force law and hence larger hysteresis loops.

Figures 6(*a*) and 6(*b*) support the hypothesis that larger hysteresis loops give rise to enhanced excess pressure. However, despite the fact that the rate of polymer stress work, $\dot{W}_p \equiv \int_V \boldsymbol{\tau}_p : \boldsymbol{\nabla u} \, \mathrm{d}V$ evaluated in CV_1 (see figure 6*c*) is a positive for all the models, its qualitative variation with *De* is similar to that of $\dot{W}_E$ depicted in figure 5(*d*). This clearly demonstrates that the pressure drop enhancement at low *b* is indeed occurring due to the enhancement of $\dot{W}_E$, whereas at high *b* it occurs because of the polymer induced flow modification captured by $\dot{W}_V$ (see figure 5*e*). Hence, at low *b* the area enclosed by the hysteresis loop indeed provides a good measure of the excess pressure drop, but at high *b* it does not.

5.5. *Vortex dynamics*

To illustrate various vortex formation pathways, representative streamline patterns have been depicted in figure 7. Overall in agreement with prior experimental findings, our simulations have revealed two vortex formation pathways: (i) at lower chain extensibility the size and the intensity of the upstream corner vortex significantly increases while the downstream corner vortex shrinks (see figure 7*a–d*) as *De* is enhanced (see figure 7*a–d*) and, (ii) at high chain extensibility, the upstream and downstream corner vortices show a slight increase and decrease in size and their intensity respectively as *De* is increased to approximately 0.25 (see figure 7*e*). Moreover, at $De \geqslant 0.25$ a reduction and enhancement of size and intensity of the upstream and downstream vortices, respectively, is observed. This event is closely followed by formation of a lip vortex (see figure 7*j*) that grows significantly with further enhancement of *De*. Finally, at $De \sim O(1)$ the lip and corner vortices merge resulting in a single large corner vortex (see figures 7*g* and 7*h*).

The variation of the measured and computed reattachment L_v of the upstream corner vortex as well as the coordinates of its centre (ζ, ξ) as a function of *De* is depicted in figure 8. Overall as *De* is enhanced, L_v increases and ζ moves away from
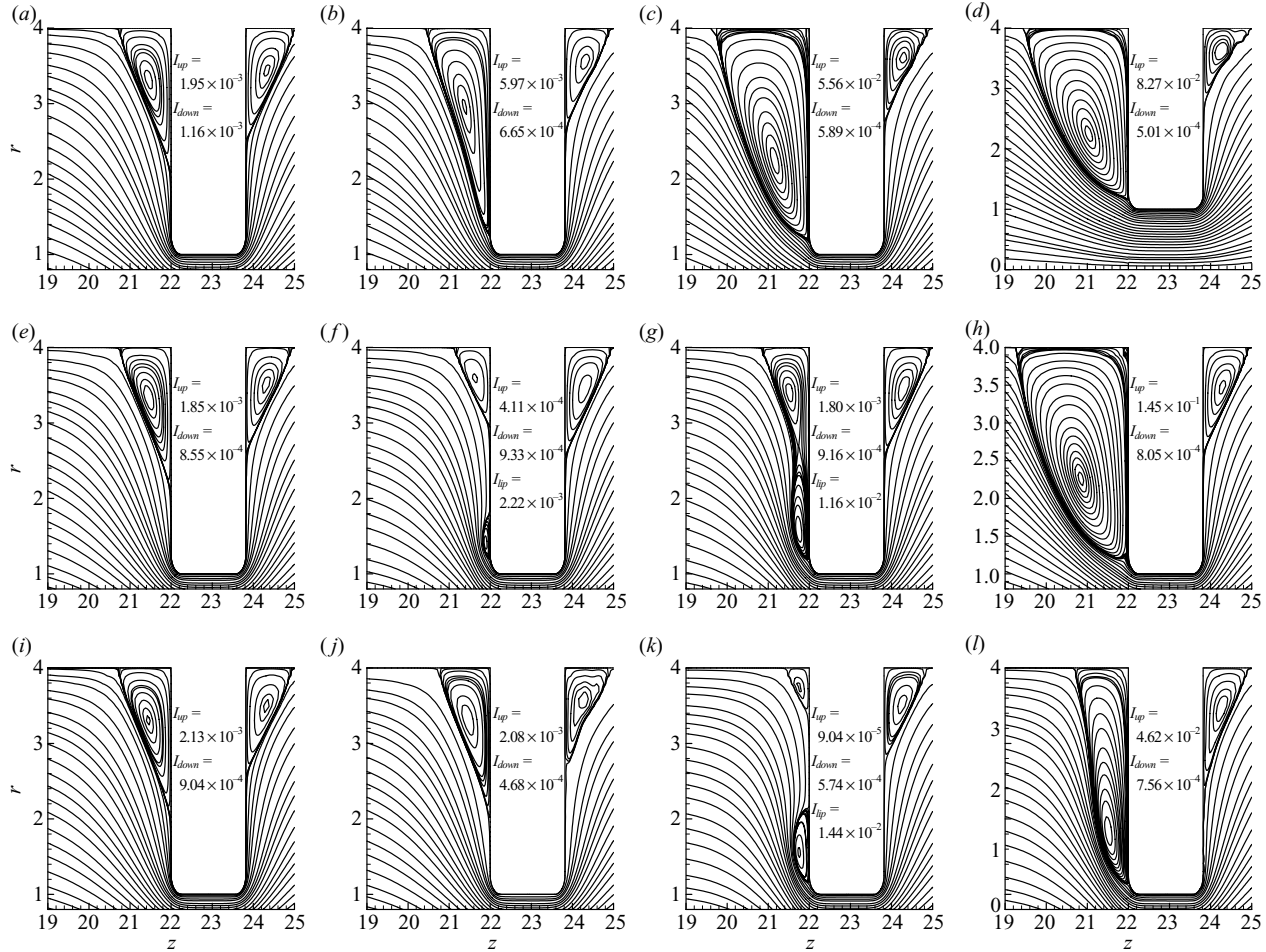
FIGURE 7. Representative streamlines patterns. Three segment bead-spring chain with $b = 225$: (a) $De = 0.087$, (b) $De = 0.304$, (c) $De = 0.45$, (d) $De = 0.5$, FENE dumbbell with $b = 1800$, (e) $De = 0.217$, (f) $De = 0.915$, (g) $De = 1.018$, (h) $De = 1.506$ and three segment FENE model with $b_{max} = 4500$, (i) $De = 0.130$, (j) $De = 0.450$, (k) $De = 0.915$, (l) $De = 1.018$.
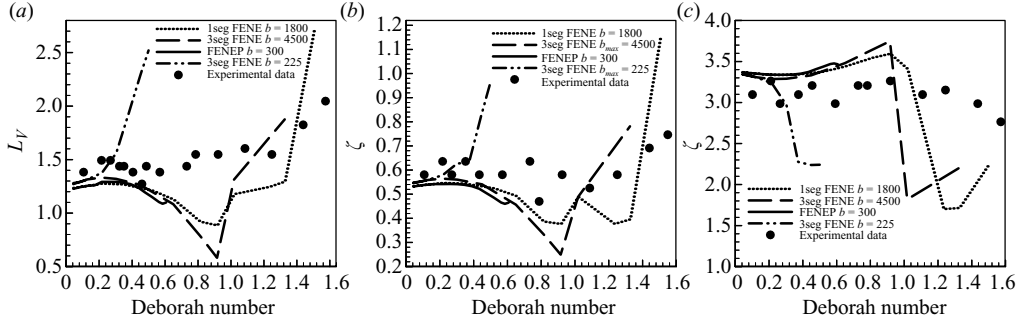
FIGURE 8. Variation of (*a*) the reattachment length (L_v) and the vortex centre coordinates (*b*) ζ and (*c*) ξ versus *De*.
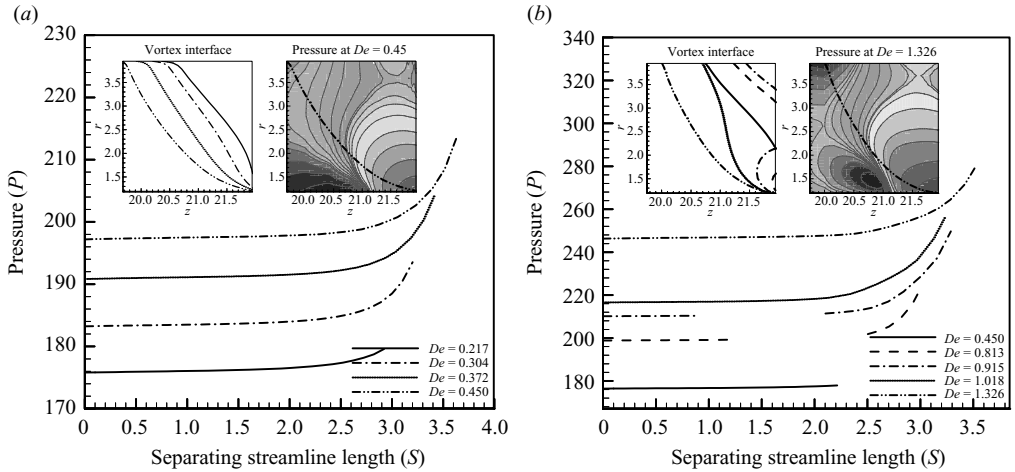

FIGURE 9. Pressure variation along separating streamlines: (*a*) three segment bead-spring chain with $b = 225$, (*b*) three segment bead-spring chain with $b = 4500$. The length of the separating streamline (S) has been set to zero at the upper wall where it originates, when a distinct lip vortex appears S continues to increase further along the vertical wall and then along the path of the separating streamline of the lip vortex.

the vertical wall while ξ shifts inward towards the axis of symmetry. A departure from this trend is observed for higher chain extensibilities at $De \sim O(1)$ when the upstream corner vortex and the lip vortex merge resulting in a corner vortex with increased L_v, yet ζ shifts downstream towards the vertical wall. Overall, the simulations with higher chain extensibility can qualitatively predict the vortex shape evolution as a function of *De*.

In order to elucidate the interplay between the chain finite extensibility and vortex evolution path, we have examined the pressure, polymer stretch and body force profiles along the interface of the upstream corner vortex and main flow. Figure 9 depicts the pressure profile at representative *De* for low and high chain extensibility along the separating streamline. In general, at all *De* the pressure increases along the path of the separating streamline S, that originates from the upper wall. However, in the case when the upstream corner vortex size is significantly larger than the Newtonian
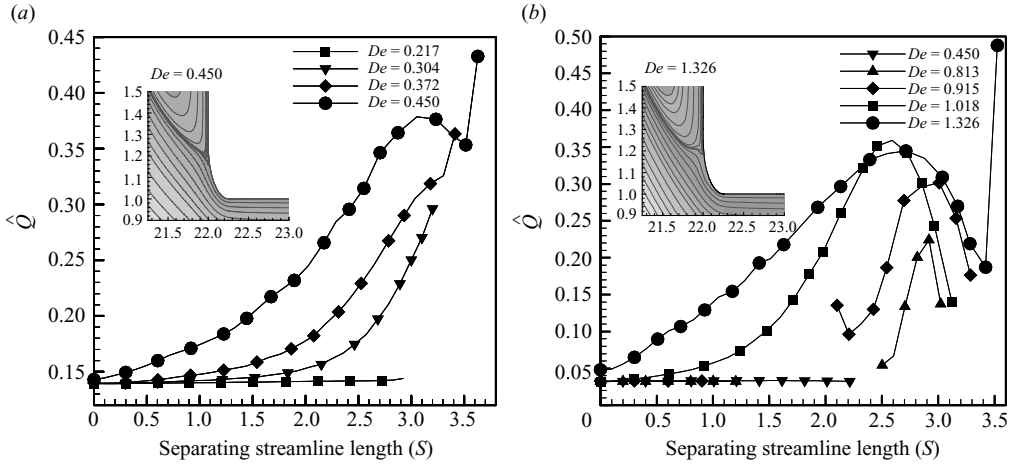
(a)

(b)

FIGURE 10. Polymer stretch variation along the separating streamlines: (*a*) three segment bead-spring chain with $b = 225$, (*b*) three segment bead-spring chain with $b = 4500$.

vortex a rather steep increase in the pressure in the proximity of the vertical wall is noticed (see figure 9*a* and *b*). A similar increase of the pressure is observed along the separating streamline when the lip vortex is present. This clearly suggests that the upstream corner vortex and lip vortex growth is primarily driven by an adverse pressure gradient. The insets of figures 9(*a*) and 9(*b*) also depict typical contour plots of the pressure inside the upstream corner vortex that further emphasize that the flow separation is caused by the adverse pressure gradient.

In creeping flows the magnitude of the adverse pressure gradient is determined by the body forces. Therefore, the variation of the excess body forces due to the polymer and the solvent relative to that of the Newtonian flow have been investigated along the separating streamline. Figures 9(*c*) and 9(*d*) depict the variation of the excess body force components F_S due to the polymer and the solvent in the flow direction. As expected, the magnitude of F_S for both the excess polymer and solvent body forces increases in all cases along S for both the corner and lip vortex. Clearly, the extent of polymer stretch determines the polymer stress and hence the polymer body force along the separating streamline. In figure 10 the polymer stretch quantified as the ensemble average of the normalized end-to-end distance ($\hat{Q} = \langle |\sum_{i=1}^{N} \boldsymbol{Q}_i| \rangle / \sqrt{b}$) of the bead-spring models is plotted against the separating streamline length S. The value of $\hat{Q}$ as a function of S remains nearly unchanged for De where vortex growth is not significant. However, at low finite extensibility, when significant upstream corner vortex growth is observed $\hat{Q}$ increases monotonically with S to a relatively high value (see figure 10*a*) resulting in a large F_S. This trend is not observed at high chain extensibility when the formation of the lip vortex is observed. In this case, $\hat{Q}$ first increases appreciably only along the lip vortex separating streamline, and then as the lip vortex coalesces with the upstream corner vortex and grows with increasing De, $\hat{Q}$ in the upstream portion of the separating streamline increases significantly along S. Overall, this analysis clearly indicates that at low chain extensibility as De is enhanced the flow microstructure coupling leads to a substantial increase in $\hat{Q}$ along the separating streamline of the corner vortex leading to substantial corner vortex growth. However, at high chain extensibilities substantial increases in $\hat{Q}$ is initially

observed near the re-entrant corner leading to formation of a lip vortex that eventually merges with the corner vortex.

6. Summary

Self-consistent multiscale flow simulations of a highly elastic dilute polymeric solution, described by first principles micromechanical models, through a 4:1:4 axisymmetric contraction and expansion geometry has been investigated. Through comparisons with experimental measurements, we have demonstrated that the pressure drop evolution as a function of the flow rate can be accurately predicted when the polymer chain dynamics is described by multi-segment bead-spring micromechanical models that closely capture the transient extensional viscosity of the experimental fluid. Specifically, for the first time the experimentally observed doubling of the dimensionless pressure drop at intermediate flow rates has been predicted. Moreover, based on an energy dissipation analysis it has been shown that the variation of the pressure drop with flow rate is controlled by the flow-microstructure coupling in the extensional flow dominated region of the flow. Specifically, it has been demonstrated that at low chain extensibility excess pressure drop occurs due to the energy dissipation caused by elastic stresses, while at high chain extensibility the excess pressure drop mainly occurs due to significant flow kinematics modification caused by presence of highly stretched polymers near the flow centreline in the vicinity of the contraction and expansion region.

Finally, the influence of the macromolecular chain extensibility on the vortex dynamics, i.e. growth of the upstream corner vortex at low maximum chain extensibility or the shrinkage of the upstream corner vortex coupled with the formation of a lip vortex that merges with the upstream corner vortex at high maximum chain extensibility has been elucidated. Specifically, it has been shown that at low chain extensibility as De is enhanced the flow microstructure coupling leads to a substantial increase in $\hat{Q}$ along the separating streamline of the corner vortex leading to substantial corner vortex growth. However, at high chain extensibilities substantial increases in $\hat{Q}$ is initially observed near the re-entrant corner leading to formation of a lip vortex that eventually merges with the corner vortex.

REFERENCES

AL-MUBAIYEDH, U. A., SURESHKUMAR, R. & KHOMAMI, B. 2000 Linear stability of viscoelastic Taylor–Couette flow: influence of fluid rheology and energetics. *J. Rheol.* **44** (5), 1121–1138.

ALVES, M. A., OLIVEIRA, P. J. & PINHO, F. T. 2004 On the effect of contraction ratio in viscoelastic flow through abrupt contractions. *J. Non-Newtonian Fluid Mech.* **122**, 117–130.

BAJAJ, M., BHAT, P. P., PRASKASH, J. R. & PASQUALI, M. 2006 Multiscale simulation of viscoelastic free surface flows. *J. Non-Newtonian Fluid Mech.* **140**, 87–107.

BINDING, D. M., PHILLIPS, P. M. & PHILLIPS, T. N. 2006 Contraction/expansion flows: the pressure drop related issues. *J. Non-Newtonian Fluid Mech.* **137**, 31–38.

BINDING, D. M. & WALTERS, K. 1988 On the use of flow through a contraction in estimating the extensional viscosity of mobile polymer solutions. *J. Non-Newtonian Fluid Mech.* **30**, 233–250.

BIRD, R. B., CURTISS, C. F., ARMSTRONG, R. C. & HASSAGER O. 1987 *Dynamics of Polymeric Liquids*, vol. 2. Wiley.

BOGER, D. V. 1987 Viscoelastic flows through contractions. *Annu. Rev. Fluid Mech.* **19**, 157–182.

BOGER, D. V. & BINNINGTON, R. J. 1990 Circular entry flows in fluid M1. *J. Non-Newtonian Fluid Mech.* **35**, 339–360.

BOGER, D. V. & BINNINGTON, R. J. 1994 Experimental removal of the re-entrant corner singularity in tubular entry flows. *J. Rheol.* **38**, 333–349.

BROOKS, A. N. & HUGHES, T. J. R. 1982 Streamline upwind/Petrov–Galerkin formulations for convection dominated flows with particular emphasis on the incompressible Navier–Stokes equations. *Comp. Methods Appl. Mech. Engng* **32**, 199–259.

CARTALOS, U. & PIAU, J. M. 1992 Creeping flow regimes of low concentration polymer solutions in thick solvents through an orifice die. *J. Non-Newtonian Fluid Mech.* **45**, 231–285.

COATES, P. J., ARMSTRONG, R. C. & BROWN, R. A. 1992 Calculation of steady-state viscoelastic flow through axisymmetric contractions with the EEME formulation. *J. Non-Newtonian Fluid Mech.* **42**, 141–188.

COGSWELL, F. N. 1972 Converging flow of polymer melts in extrusion dies. *Polym. Engng Sci.* **12**, 64–73.

EISENBRAND, G. D. & GODDARD, J. D. 1982 Birefringence and pressure drop for the orifice flow of a polymer solution. *J. Non-Newtonian Fluid Mech.* **11**, 37–52.

GRILLET, A. M., YANG, B., KHOMAMI, B. & SAHQFEH, E. G. 1999 Modelling of viscoelastic lid driven cavity flow using finite element simulations. *J. Non-Newtonian Fluid Mech.* **88**, 99–131.

GUENETTE, R. & FORTIN, M. 1995 A new mixed finite element method for computing viscoelastic flows. *J. Non-Newtonian Fluid Mech.* **60**, 27–52.

HALIN, P., LIELENS, G., KEUNINGS, R. & LEGAT, V. 1998 The Lagrangian particle method for macroscopic and micro–macro viscoelastic flow computations. *J. Non-Newtonian Fluid Mech.* **79**, 387–403.

HAPPEL, J. & BRENNER, H. 1965 *Low Reynolds Number Hydrodynamics.* Prentice-Hall.

HU, X., DING, Z. & LEE, L. J. 2005 Simulation of two-dimensional transient visoelastic flow using the CONNFFESSIT approach. *J. Non-Newtonian Fluid Mech.* **127**, 107–122.

HUA, C. C. & SCHIEBER, J. D. 1998 Viscoelastic flow through fibrous media using the CONNFFESSIT approach. *J. Rheol.* **42** (3), 477–491.

HULSEN, M. A., VAN HEEL, A. P. G. & VAN DEN BRULE, B. H. A. A. 1997 Simulation of viscoelastic flows using Brownian configuration fields. *J. Non-Newtonian Fluid Mech.* **70**, 79–101.

JAMES, D. F. & CHANDLER, G. M. 1990 Measurement of the extensional viscosity of M1 in a converging channel rheometer. *J. Non-Newtonian Fluid Mech.* **35**, 445–458.

KEILLER, R. A. 1993 Entry-flow calculations for the Oldroyd-B and FENE equations. *J. Non-Newtonian Fluid Mech.* **46**, 143–178.

KEUNINGS, R. 2004 Micro–macro methods for the multiscale simulation of viscoelastic flow using molecular models of kinetic theory. In *Rheology Reviews* (ed. D. M. Binding & K. Walters), pp. 67–98. British Society of Rheology.

KHOMAMI, B., TALWAR, K. K. & GANPULE, H. K. 1994 A comparative study of higher and lower order finite element techniques for computation of viscoelastic flows. *J. Rheol.* **38**, 255–289.

KIM, J. M., KIM, C., KIM, J. H., CHUNG, C., AHN, K. H. & LEE, S. J. 2005 High resolution finite element simulation of 4:1 planar contraction flow of a viscoelastic fluid. *J. Non-Newtonian Fluid Mech.* **129**, 23–37.

KOPPOL, A. P. 2007 Dynamics and frictional drag behaviour of viscoelastic flows in complex geometries: a multiscale simulation approach. DSc thesis, Washington University, St. Louis.

KOPPOL, A. P., SURESHKUMAR, R. & KHOMAMI, B. 2007 An efficient algorithm for multiscale flow simulation of dilute polymeric solutions using bead-spring chains. *J. Non-Newtonian Fluid Mech.* **141**, 180–192.

LARSON, R. G. 2005 The rheology of dilute solutions of flexible polymers: progress and problems. *J. Rheol.* **49**, 1–70.

LASO, M. & ÖTTINGER, H. C. 1993 Calculation of viscoelastic flow using molecular models: the CONNFFESSIT approach. *J. Non-Newtonian Fluid Mech.* **47**, 1–20.

LASO, M., PICASSO, M. & ÖTTINGER, H. C. 1997 two-dimensional time dependent viscoelastic flow calculations using CONNFFESSIT. *AIChE J.* **43**, 877–892.

LAWLER, J. V., MULLER, S. J., BROWN, R. A. & ARMSTRONG, R. C. 1986 Laser Doppler velocimetry measurements of velocity fields and transitions in viscoelastic fluids. *J. Non-Newtonian Fluid Mech.* **20**, 51–92.

LEE, A. G., SHAQFEH, E. S. G. & KHOMAMI, B. 2002 A study of viscoelastic free surface flows by the finite element method: Hele–Shaw and slot coating flows. *J. Non-Newtonian Fluid Mech.* **108**, 327–362.

LI, J., BURGHARDT, W. R., YANG, B. & KHOMAMI, B. 1998 Flow birefringence and computational studies of a shear thinning polymer solution in axisymmetric stagnation flow. *J. Non-Newtonian Fluid Mech.* **74**, 151–193.

LI, J., BURGHARDT, W. R., YANG, B. & KHOMAMI, B. 2000 Birefringence and computational studies of a polystyrene Boger fluid in axisymmetric stagnation flow. *J. Non-Newtonian Fluid Mech.* **91**, 189–220.

MCKINLEY, G. H., RAIFORD, W. P., BROWN, R. A. & ARMSTRONG, R. C. 1991 Nonlinear dynamics of viscoelastic flow in axisymmetric abrupt contractions. *J. Fluid Mech.* **223**, 411–456.

MOMPEAN, G. & DEVILLE, M. 1997 Unsteady finite volume simulation of Oldroyd-B fluid through a three-dimensional planar contraction. *J. Non-Newtonian Fluid Mech.* **72**, 253–279.

NIGEN, S. & WALTERS, K. 2002 Viscoelastic contraction flows: comparison of axisymmetric and planar configurations. *J. Non-Newtonian Fluid Mech.* **102**, 343–359.

OLIVEIRA, M. S. N., OLIVEIRA, P. J., PINHO, F. T. & ALVES, M. A. 2007 Effect of contraction ratio upon viscoelastic flow in contractions: the axisymmetric case. *J. Non-Newtonian Fluid Mech.* **147**, 92–108.

ÖTTINGER, H. C., VAN DEN BRULE, B. H. A. A. & HULSEN, M. A. 1997 Brownian configuration fields and variance reduce CONNFFESSIT. *J. Non-Newtonian Fluid Mech.* **70**, 255–261.

PHILIPS, T. N. & SMITH, K. D. 2006 A spectral element approach to the simulation of viscoelastic flows. *J. Non-Newtonian Fluid Mech.* **138**, 98–110.

PURNODE, B. & CROCHET, M. J. 1996 Flows of polymer solutions through contractions. Part 1: flows of polyacrylamide solutions through planar contractions. *J. Non-Newtonian Fluid Mech.* **65**, 269–289.

RALLISON, J. M. & HINCH, E. J. 2004 The flow of an Oldroyd fluid past a re-entrant corner: the downstream boundary layer. *J. Non-Newtonian Fluid Mech.* **116**, 141–162.

RENARDY, M. 1997 Re-entrant corner behaviour of the PTT fluid. *J. Non-Newtonian Fluid Mech.* **69**, 99–104.

ROTHSTEIN, J. P. & MCKINLEY, G. H. 1999 Extensional flow of a polystyrene Boger fluid through a 4:1:4 contraction/expansion. *J. Non-Newtonian Fluid Mech.* **86**, 61–88.

ROTHSTEIN, J. P. & MCKINLEY, G. H. 2001 The axisymmetric contraction-expansion: the role of extensional rheology on vortex growth dynamics and the enhanced pressure drop. *J. Non-Newtonian Fluid Mech.* **98**, 33–63.

ROTHSTEIN, J. P. & MCKINLEY, G. H. 2002 Inhomogeneous transient uniaxial extensional rheometry. *J. Rheol.* **46**, 1419–1443.

SHAQFEH, E. S. G. 2005 The dynamics of single-molecule DNA in flow. *J. Non-Newtonian Fluid Mech.* **130**, 1–28.

SMITH, M. D., ARMSTRONG, R. C., BROWN, R. A. & SURESHKUMAR, R. 2000 Finite element analysis of stability of two-dimensional viscoelastic flows to three-dimensional perturbations. *J. Non-Newtonian Fluid Mech.* **93**, 203–244.

SOMASI, M. & KHOMAMI, B. 2000 Linear stability and dynamics of viscoelastic flows using time-dependent stochastic simulation techniques. *J. Non-Newtonian Fluid Mech.* **93**, 339–362.

SOMASI, M. & KHOMAMI, B. 2001 A new approach for studying the hydrodynamic stability of fluids with microstructure. *Phys. Fluids* **13**, 1811–1814.

SOMASI, M., KHOMAMI, B., WOO, N. J., HUR, J. S. & SHAQFEH, E. S. G. 2002 Brownian dynamics simulations of bead-rod and bead-spring chains: numerical algorithms and coarse-graining issues. *J. Non-Newtonian Fluid Mech.* **108**, 227–255.

SZABO, B. & BABUSKA, I. 1987 *Finite Element Analysis.* Wiley.

SZABO, P., RALLISON, J. M. & HINCH, E. J. 1997 Start up of flow of a FENE-fluid through a 4:1:4 constriction in a tube. *J. Non-Newtonian Fluid Mech.* **72**, 73–86.

TALWAR, K. K., GANPULE, H. K. & KHOMAMI, B. 1994 A note on the selection of spaces in computation of viscoelastic flows using the hp-finite element method. *J. Non-Newtonian Fluid Mech.* **52**, 293–307.

TALWAR, K. K. & KHOMAMI, B. 1992 Application of higher order finite element methods to viscoelastic flow in porous media. *J. Rheol.* **36**, 1377–1416.

WAPPEROM, P., KEUNINGS, R. & LEGAT, V. 2000 The backward-tracking Lagrangian particle method for transient viscoelastic flows. *J. Non-Newtonian Fluid Mech.* **91**, 273–295.

WIEST, J. M. & TANNER, R. I. 1989 Rheology of bead-nonlinear spring chain macromolecules. *J. Rheol.* **33** (2), 281–316.

YANG, B. & KHOMAMI, B. 1999 Simulation of sedimentation of a sphere in a viscoelastic fluid using molecular based constitutive models. *J. Non-Newtonian Fluid Mech.* **82**, 429–452.